Twisted Bilayer Graphene: A Phonon-Driven Superconductor

Biao Lian,[1] Zhijun Wang,[2,3] and B. Andrei Bernevig[4,5,6]
[1]Princeton Center for Theoretical Science, Princeton University, Princeton, New Jersey 08544, USA
[2]Beijing National Laboratory for Condensed Matter Physics, and Institute of Physics, Chinese Academy of Sciences, Beijing 100190, China
[3]University of Chinese Academy of Sciences, Beijing 100049, China
[4]Department of Physics, Princeton University, Princeton, New Jersey 08544, USA
[5]Dahlem Center for Complex Quantum Systems and Fachbereich Physik, Freie Universitat Berlin, Arnimallee 14, 14195 Berlin, Germany
[6]Max Planck Institute of Microstructure Physics, 06120 Halle, Germany

(Received 31 July 2018; revised manuscript received 19 January 2019; published 28 June 2019; corrected 5 June 2020)

We study the electron-phonon coupling in twisted bilayer graphene (TBG), which was recently experimentally observed to exhibit superconductivity around the magic twist angle $\theta \approx 1.05°$. We show that phonon-mediated electron attraction at the magic angle is strong enough to induce a conventional intervalley pairing between graphene valleys K and K' with a superconducting critical temperature $T_c \sim 1$ K, in agreement with the experiment. We predict that superconductivity can also be observed in TBG at many other angles θ and higher electron densities in higher moiré bands, which may also explain the possible granular superconductivity of highly oriented pyrolytic graphite. We support our conclusions by *ab initio* calculations.

DOI: 10.1103/PhysRevLett.122.257002

Twisted bilayer graphene (TBG) is a highly tunable system, which is engineered by stacking two graphene layers at a relative twist angle θ, a procedure which produces a moiré pattern superlattice. Recently [1,2], it was observed that TBG at low filling exhibits unconventional insulator and superconductor phases near the magic angle $\theta = 1.05°$, where the lowest electron bands become extremely flat [3,4]. The Fermi energy of the system is below 10 meV, while by comparison the superconductor critical temperature $T_c \sim 1$ K is relatively high. Since then, some theoretical studies have been devoted to understanding the insulator and superconductor phases of the TBG [5–34]. A closely related system, the highly oriented pyrolytic graphite (HOPG), which contains numerous twisted interfaces, was also reported showing evidences of granular superconductivity [35–37], and is suggested to share a similar superconductivity mechanism as that in TBG [9,38].

Here we show that the TBG moiré pattern exhibits an enhanced electron-phonon coupling, which can lead to a conventional superconductivity with high T_c at certain twist angles and electron densities. In particular, our calculation estimates a T_c of order 1 K at the magic angle $\theta = 1.05°$ around a filling of two electrons per superlattice unit cell, in agreement with the TBG experiment [1]. Most importantly, we make the falsifiable prediction that T_c can be higher at larger electron densities and certain ranges of the twist angle θ, for instance in the *second moiré* band near $\theta = 0.6°$, and in the *second or higher moiré bands* for $\theta \gtrsim 1°$. This may explain the possible superconductivity of HOPG where the interface twist angles are mostly not at the magic angle. Further, we conjecture the insulating phase at two electrons per unit cell is a Bose-Mott insulator [39].

The moiré superlattice of TBG is shown in Fig. 1(a), where $\boldsymbol{D}_1$ and $\boldsymbol{D}_2$ are lattice vectors of length $|\boldsymbol{D}_j| = a_0/[2\sin(\theta/2)]$, and $a_0 = 0.246$ nm is the graphene lattice constant. The large electron-phonon coupling of TBG can be intuitively understood from Fig. 1. We denote the phonon field in TBG layer j ($j = 1, 2$) as $\mathbf{u}^{(j)}(\mathbf{r})$, namely, the atomic displacement at coordinate $\mathbf{r}$ in layer j. We then define the relative displacement $\mathbf{u} = \mathbf{u}^{(1)} - \mathbf{u}^{(2)}$, and the center of mass displacement $\mathbf{u}_c = (\mathbf{u}^{(1)} + \mathbf{u}^{(2)})/2$. The key observation is that for small θ, a small in plane relative

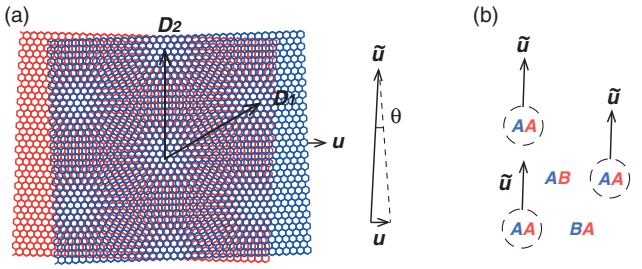

FIG. 1. (a) Moiré pattern of the TBG, which has AA, AB, and BA stacking sites (A and B denote the graphene sublattices). (b) A uniform displacement $\mathbf{u}$ of graphene layer 1 (blue) relative to layer 2 (red) yields a superlattice displacement $|\tilde{\mathbf{u}}| = \gamma|\mathbf{u}|$ perpendicular to $\mathbf{u}$, where $\gamma = 1/2\tan(\theta/2)$.

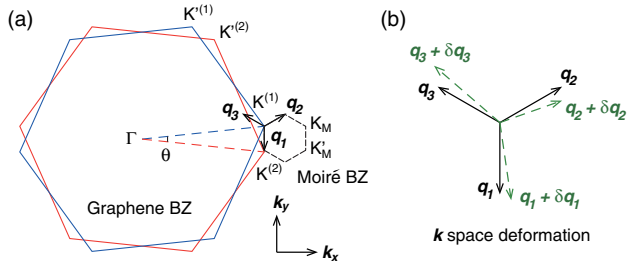

FIG. 2. (a) Illustration of the graphene BZs of two layers, and their relation to the moiré BZ. (b) Under phonon-induced superlattice deformations, $\mathbf{q}_j$, are deformed, which leads to the change in electron band energies.

displacement $\mathbf{u}$ significantly affects the superlattice. When layer 1 of the TBG undergoes a uniform translation $\mathbf{u}$ relative to layer 2 [Fig. 1(a)], the AA stacking positions will move by $|\tilde{\mathbf{u}}| = \gamma|\mathbf{u}|$ perpendicular to $\mathbf{u}$, where $\gamma = 1/[2\tan(\theta/2)]$ [Fig. 1(b)]. If the relative displacement $\mathbf{u}$ is nonuniform, it will induce a large superlattice deformation due to the amplification factor $\gamma \approx \theta^{-1} \gg 1$ (see the Supplemental Material [40] Sec. I). Accordingly, the low energy electrons will experience a large variation of superlattice potential, yielding a strong coupling with the in plane relative displacement phonon field $\mathbf{u}$. In contrast, the center of mass displacement $\mathbf{u}_c$ has no amplified effect on the superlattice (see the Supplemental Material [40] Sec. I). Therefore, we shall only focus on the electron-phonon coupling of the relative displacement field $\mathbf{u}$.

The band structure of the TBG can be calculated using the continuum model in Ref. [4]. Figure 2(a) shows the graphene Brillouin zones (BZs) of the two layers, which are relatively twisted by θ. When the two layers are decoupled, the low energy electrons of each layer are Dirac fermions at K and K' points, which are described by Hamiltonian $h^K(\mathbf{k}) = v(\sigma_x k_x - \sigma_y k_y) = \hbar v \boldsymbol{\sigma}^* \cdot \mathbf{k}$ and $h^{K'}(\mathbf{k}) = -\hbar v \boldsymbol{\sigma} \cdot \mathbf{k}$, respectively. Here $\sigma_{x,y,z}$ are the Pauli matrices for sublattice indices, $\hbar v \approx 610$ meV nm is the graphene Fermi velocity, and momentum $\mathbf{k}$ is measured from the Dirac point. In addition, each Dirac band has a twofold spin degeneracy, and we assume zero spin orbit coupling. The K (K') points of the two layers differ by momentum vectors $\mathbf{q}_j$ ($-\mathbf{q}_j$) as shown in Fig. 2(a) ($j = 1, 2, 3$), which constitute the edges of the hexagonal superlattice moiré BZ, with $|\mathbf{q}_j| = k_\theta = 8\pi \sin(\theta/2)/3a_0$.

When the interlayer hopping is introduced, to the lowest order, the Hamiltonian at valley K and near moiré BZ K'_M point [Fig. 2(a)] takes the truncated form [4]

$$H^K(\mathbf{k}) = \begin{pmatrix} h^K(\mathbf{k}) & wT_1 & wT_2 & wT_3 \\ wT_1^\dagger & h^K(\mathbf{k}_1) & 0 & 0 \\ wT_2^\dagger & 0 & h^K(\mathbf{k}_2) & 0 \\ wT_3^\dagger & 0 & 0 & h^K(\mathbf{k}_3) \end{pmatrix}, \quad (1)$$

where $\mathbf{k}$ is measured from K'_M point, $\mathbf{k}_j = \mathbf{k} - \mathbf{q}_j$ ($j = 1, 2, 3$), the matrices T_j are given by $T_1 = 1 + \sigma_x$, $T_2 = 1 - \frac{1}{2}\sigma_x - (\sqrt{3}/2)\sigma_y$, $T_3 = 1 - \frac{1}{2}\sigma_x + (\sqrt{3}/2)\sigma_y$, and $w \approx 110$ meV is the nearest momentum hopping amplitude. Near $\mathbf{k} = 0$ and zero energy, the Hamiltonian [Eq. (1)] can be folded into a 2×2 effective Dirac Hamiltonian [4]

$$\tilde{H}^K(\mathbf{k}) = \left(\frac{1 - 3\alpha^2}{1 + 6\alpha^2}\right) \hbar v \boldsymbol{\sigma}^* \cdot \mathbf{k}, \quad (2)$$

where $\alpha = w/\hbar v k_\theta$. In total, there are 4 Dirac fermions at K'_M and four Dirac fermions at K_M near zero energy, due to the valley K, K' and spin $\uparrow, \downarrow$ fourfold degeneracy [further momentum hoppings are needed in Eq. (1) to obtain the Dirac fermions at K_M]. The Dirac fermions at valley K' have opposite helicity, described by replacing $\boldsymbol{\sigma}^* \cdot \mathbf{k} \to \boldsymbol{\sigma} \cdot \mathbf{k}$ in Eq. (2). The magic angle $\theta \approx 1.05°$ is given by $\alpha^2 = 1/3$, where the Dirac Fermi velocity vanishes. Numerical calculations near the magic angle show the entire width of the lowest two bands can be as low as 1 meV [4].

The coupling between electrons and long wavelength phonons can be obtained by examining the change of electron band energies under uniform lattice deformations. Under deformation induced by a relative displacement $\mathbf{u}$, the momentum vectors $\mathbf{q}_j$ [Fig. 2(b)] are deformed by $\delta\mathbf{q}_1 = \gamma k_\theta(\partial_x u_x, \partial_y u_x)$, and $\delta\mathbf{q}_{2,3} = \gamma k_\theta[\pm(\sqrt{3}/2)\partial_x u_y - \frac{1}{2}\partial_x u_x, -\frac{1}{2}\partial_y u_x \pm (\sqrt{3}/2)\partial_y u_y]$ (see the Supplemental Material [40] Sec. I). This induces a change of $\mathbf{k}_j = \mathbf{k} - \mathbf{q}_j$ in the Hamiltonian [Eq. (1)], which perturbs the electron band energies. The variations of v and w are subleading compared to $\delta\mathbf{q}_j$, and will be ignored here. The variation in Hamiltonian [Eq. (2)], namely, the electron-phonon coupling, $\delta\tilde{H}(\bar{\mathbf{k}}) = H_{\rm ep}(\bar{\mathbf{k}})$, can be derived to be (see the Supplemental Material [40] Sec. I)

$$\begin{aligned} H_{\rm ep}^{\eta,\zeta,s}(\bar{\mathbf{k}}) &= H_{C3}^{\eta,\zeta,s}(\bar{\mathbf{k}}) + H_{{\rm SO}(2)}^{\eta,\zeta,s}(\bar{\mathbf{k}}), \\ H_{C3}^{\eta,\zeta,s}(\bar{\mathbf{k}}) &= g_{1\alpha}\eta\gamma\hbar v \psi^\dagger_{\mathbf{k}'}[\bar{k}_x(\partial_y u_x + \partial_x u_y) \\ &\quad + \bar{k}_y(\partial_x u_x - \partial_y u_y)]\psi_{\mathbf{k}}, \\ H_{{\rm SO}(2)}^{\eta,\zeta,s}(\bar{\mathbf{k}}) &= \gamma\hbar v \psi^\dagger_{\mathbf{k}'}[g_{2\alpha}(\eta\sigma_x\bar{k}_x - \sigma_y\bar{k}_y)(\partial_y u_x - \partial_x u_y) \\ &\quad + g_{3\alpha}(\eta\sigma_x\bar{k}_y + \sigma_y\bar{k}_x)(\partial_x u_x + \partial_y u_y)]\psi_{\mathbf{k}}, \end{aligned} \quad (3)$$

with index $\eta = \pm 1$ for graphene valley K, K', $\zeta = \pm 1$ for moiré BZ valley K_M, K'_M, $s = \pm 1$ for spin $\uparrow, \downarrow$, and we have defined $g_{1\alpha} = \{[9\alpha^2(1 + 3\alpha^2)]/(1 + 6\alpha^2)^2\}$, $g_{2\alpha} = [(9\alpha^2)/(1 + 6\alpha^2)^2]$, and $g_{3\alpha} = [(3\alpha^2)/(1 + 6\alpha^2)]$. $\psi_{\mathbf{k}}$ and $\psi^\dagger_{\mathbf{k}}$ are the Dirac electron annihilation and creation operators, and $\bar{\mathbf{k}} = (\mathbf{k} + \mathbf{k}')/2$ is the average momentum of the electron state before and after phonon interaction. Note that $H_{\rm ep}$ is independent of ζ and s, and contains two parts H_{C3} and $H_{{\rm SO}(2)}$, which are C_{3z} and SO(2) rotationally invariant about z axis, respectively. Besides, $H_{\rm ep}$ respects

the TBG twofold rotation symmetry C_{2x} about x axis, which transforms (u_x, u_y) to $(-u_x, u_y)$.

We also need to know the phonon spectrum of the TBG. Previous studies show that in plane phonons of the two layers of TBG are nearly decoupled [48]. Therefore, the TBG in plane phonon spectrum is approximately that of two isolated graphene monolayers folded into the moiré BZ. The lowest bands of phonon field $\mathbf{u}$ thus has Hamiltonian

$$H_{\rm ph} = \sum_{\mathbf{p}} (\hbar\omega_{\mathbf{p},L} a^\dagger_{\mathbf{p},L} a_{\mathbf{p},L} + \hbar\omega_{\mathbf{p},T} a^\dagger_{\mathbf{p},T} a_{\mathbf{p},T}), \quad (4)$$

where $a_{\mathbf{p},L}$, $a^\dagger_{\mathbf{p},L}$ and $a_{\mathbf{p},T}$, $a^\dagger_{\mathbf{p},T}$ are the annihilation and creation operators of longitudinal and transverse polarized phonons, respectively. The frequencies $\omega_{\mathbf{p},L} = c_L p$ and $\omega_{\mathbf{p},T} = c_T p$ are acoustic, with $p = |\mathbf{p}|$. c_L, c_T are the longitudinal and transverse sound speeds of monolayer graphene. The phonon field $\mathbf{u}$ at long wavelengths is

$$\mathbf{u}(\mathbf{r}) = \sum_{\mathbf{p}} \frac{e^{i\mathbf{p}\cdot\mathbf{r}}}{\sqrt{N_s \Omega_s}} (i\hat{\mathbf{p}} u_{\mathbf{p},L} + i\hat{\mathbf{z}} \times \hat{\mathbf{p}} u_{\mathbf{p},T}), \quad (5)$$

where $u_{\mathbf{p},\chi} = \sqrt{[(\hbar\Omega)/(2M\omega_{\mathbf{p},\chi})]}(a_{\mathbf{p},\chi} + a^\dagger_{-\mathbf{p},\chi})$ for $\chi = L$, T polarizations, Ω and Ω_s are the unit cell areas of the graphene lattice and moiré superlattice, respectively, and N_s is the number of supercells. There are also many optical phonon bands in the moiré BZ corresponding to short wavelength components of $\mathbf{u}$, but here we will only focus on the lowest acoustic phonon bands which couple to electrons via Eq. (3).

Assume the Fermi surfaces are $|\mathbf{k}| = k_F$ in the Dirac hole (or electron) bands. The phonon mediated electron-electron interaction near the Fermi surfaces can then be calculated perturbatively in the Bardeen-Cooper-Schrieffer (BCS) channel:

$$H^{(\rm ph)}_{\rm int} = \sum_{\mathbf{k},\mathbf{k}'} \frac{V^{II'}_{\mathbf{k}\mathbf{k}'}(\omega)}{N_s \Omega_s} c^\dagger_{\mathbf{k}',I} c^\dagger_{-\mathbf{k}',I'} c_{-\mathbf{k},I'} c_{\mathbf{k},I}, \quad (6)$$

where $I = (\eta, \zeta, s)$ denotes indices for the eight Dirac cones, the frequency $\omega = (\xi_{\mathbf{k}'} - \xi_{\mathbf{k}})/\hbar$ with $\xi_{\mathbf{k}} = -[(1-3\alpha^2)/(1+6\alpha^2)]\hbar v(|\mathbf{k}| - k_F)$ being the band energy at $\mathbf{k}$, while $c_{\mathbf{k},I}$ and $c^\dagger_{\mathbf{k},I}$ are electron annihilation and creation operators in the Dirac hole band I. To simplify the result, we take the approximation $c_L = c_T$ (both around 10^4 m/s). For θ near the magic angle ($\alpha^2 \approx 1/3$), we find the interaction in the lowest two moiré bands is

$$\frac{V^{II'}_{\mathbf{k}\mathbf{k}'}(\omega)}{\Omega_s} \approx \frac{\hbar^2 v^2 k_F^2 \varpi^{\eta\eta'}_{\mathbf{k}\mathbf{k}'}}{9Mc_T^2} \frac{\omega^2_{\mathbf{p},T}}{\omega^2 - \omega^2_{\mathbf{p},T}} f_{\eta\eta'}(\varphi_{\mathbf{k}}, \varphi_{\mathbf{k}'}), \quad (7)$$

where M is the Carbon atomic mass, $\mathbf{p} = \mathbf{k} - \mathbf{k}'$, $\varphi_{\mathbf{k}} = \arg(k_x + ik_y)$ is the polar angle of $\mathbf{k}$, and $\varpi^{\eta\eta'}_{\mathbf{k}\mathbf{k}'} = \phi^{\eta\dagger}_{\mathbf{k}'} \phi^{\eta}_{\mathbf{k}} \phi^{\eta'\dagger}_{-\mathbf{k}'} \phi^{\eta'}_{-\mathbf{k}}$ with $\phi^\eta_{\mathbf{k}} = (1, -\eta e^{-i\eta\varphi_{\mathbf{k}}})^T/\sqrt{2}$ being the Dirac hole band wave function at valley η. The function $f_{\eta\eta'}$ is given by

$$f_{\eta\eta'}(\varphi_{\mathbf{k}}, \varphi_{\mathbf{k}'}) = \begin{cases} -1 - 2\cos(\varphi_{\mathbf{k}} - \varphi_{\mathbf{k}'}), & (\eta = \eta') \\ \left| 1 - \eta \dfrac{e^{2i\varphi_{\mathbf{k}}} - e^{2i\varphi_{\mathbf{k}'}}}{e^{-i\varphi_{\mathbf{k}}} - e^{-i\varphi_{\mathbf{k}'}}} \right|^2 & (\eta = -\eta'). \end{cases} \quad (8)$$

The interaction $V^{II'}_{\mathbf{k}\mathbf{k}'}(\omega)$ is independent of spin s and moiré valley ζ.

At low energies $|\omega| < \omega_{\mathbf{p},T}$, $f_{\eta,-\eta} > 0$ indicates the intervalley interaction between K and K' ($\eta = -\eta'$) is attractive. In contrast, $f_{\eta,\eta}$ is on-average negative, and one can prove that the intravalley interaction ($\eta = \eta'$) is repulsive in all pairing channels (see the Supplemental Material [40] Sec. II C). This is due to the fact that the hole (or electron) band projections of $H^{\eta,\zeta,s}_{C3}$ and $H^{\eta,\zeta,s}_{SO(2)}$ in Eq. (3) are odd and even under $\mathbf{k}, \mathbf{k}' \to -\mathbf{k}, -\mathbf{k}'$, or under $\eta \to -\eta$, respectively (see the Supplemental Material [40] Sec. II C). Assume an electron state (wave packet) $|\bar{\mathbf{k}}_{K,\zeta,s}\rangle$ around momentum $\bar{\mathbf{k}}$ at valley K experiences a phonon-induced lattice potential $\langle H^{K,\zeta,s}_{C3}(\bar{\mathbf{k}})\rangle + \langle H^{K,\zeta,s}_{SO(2)}(\bar{\mathbf{k}})\rangle = U_{C3} + U_{SO(2)}$. By symmetry, the state $|-\bar{\mathbf{k}}_{K,\zeta',s'}\rangle$ at the same valley K will feel a potential $-U_{C3} + U_{SO(2)}$, while the state $|-\bar{\mathbf{k}}_{K',\zeta',s'}\rangle$ in the opposite valley K' will feel a potential $U_{C3} + U_{SO(2)}$. Therefore, two electrons $|\bar{\mathbf{k}}_{K,\zeta',s'}\rangle$ and $|-\bar{\mathbf{k}}_{K',\zeta',s'}\rangle$ in opposite valleys feel the same phonon-induced lattice potential, which induces an effective attraction between them. In contrast, two electrons $|\bar{\mathbf{k}}_{K,\zeta',s'}\rangle$ and $|-\bar{\mathbf{k}}_{K,\zeta',s'}\rangle$ in the same valley K feel different potentials and, thus, have a weaker or even absent attraction. Therefore, the intervalley Cooper pairing is preferred.

Since the interaction is degenerate with respect to indices ζ and s, the intervalley pairing is not yet unique. Here we simply assume the pairing is time reversal invariant, which is generically more robust under nonmagnetic disorders [49]. This yields an intervalley pairing amplitude of the form (see the Supplemental Material [40] Sec. III)

$$\Delta^{\eta\eta',\zeta\zeta',ss'}_{\mathbf{k}} = s\delta_{s,-s'}\delta_{\zeta,-\zeta'}\delta_{\eta,-\eta'}\tilde{\Delta}(\eta\mathbf{k}), \quad (9)$$

where $\tilde{\Delta}(\mathbf{k})$ is a real function of $\varphi_{\mathbf{k}} = \arg(k_x + ik_y)$. Numerically, $\tilde{\Delta}(\mathbf{k})$ can be solved and has the shape shown in Fig. 3(c), which is nodeless and dominated by an s wave. We note that an earlier optical phonon study [13] obtained both s wave and d wave, while a recent atomistic study supports s wave [50].

Substituting the realistic parameters into Eq. (7) and taking $k_F \sim k_\theta$, we find that the phonon mediated intervalley attraction is of order $-V^{II'}_{\mathbf{k}\mathbf{k}'}(0)/\Omega_s \sim 1$ meV around the magic angle, which is comparable to the Fermi energy ϵ_F and the Debye frequency of acoustic moiré phonon bands $\hbar\omega_D \sim \hbar c_T k_\theta \approx 2$ meV. When the optical phonon contributions are included, the attraction could be further

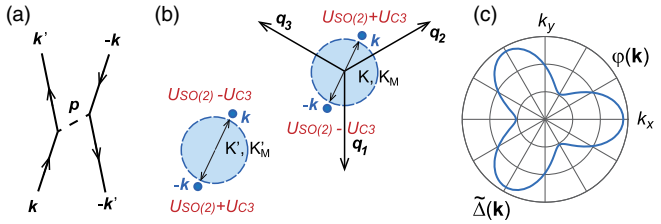

FIG. 3. (a) The process two electrons of momentum $\mathbf{k}$ and $-\mathbf{k}$ exchanges a phonon of momentum $\mathbf{p} = \mathbf{k}' - \mathbf{k}$, which mediates the electron-electron interaction in Eq. (7). (b) Illustration of phonon-induced potentials for electrons at valleys K and K' (which can be in different moiré valleys or the same moiré valley), where U_S and $\pm U_{C3}$ are contributed by $H^{\eta,\zeta,s}_{\mathrm{SO}(2)}$ and $H^{\eta,\zeta,s}_{C3}$, respectively. The dashed circles represent the Fermi surfaces. (c) Intervalley pairing $\tilde{\Delta}(\mathbf{k})$ solved numerically as a function of $\varphi(\mathbf{k})$, which is s wave (see the Supplemental Material [40] Sec. III).

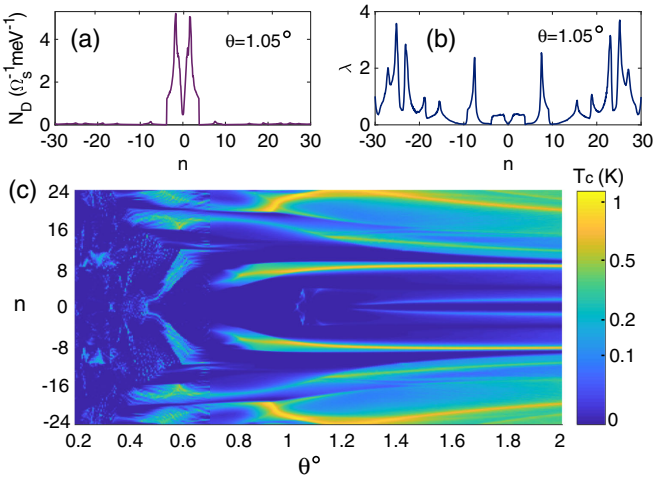

FIG. 4. (a) The density of states N_D as a function of number of electrons per superlattice unit cell n, showing the lowest conduction and valence bands are pretty flat. (b) The estimated BCS coupling strength $\lambda \approx N_D |V_{\mathbf{k}\mathbf{k}'}(0)|$ as a function of n. (c) The superconducting T_c with respect to n and θ estimated from the McMillan formula.

enhanced. Since the density of states (DOS) is as large as $N_D \gtrsim 1$ meV^{-1} Ω_s^{-1} at the magic angle, the BCS coupling strength $\lambda \approx N_D |V^{II'}_{\mathbf{k}\mathbf{k}'}| \gtrsim 1$ is strong. The screened Coulomb interaction takes the form $\mathcal{V}_e(q) = 2\pi e^2/q\epsilon(q)$, where $\epsilon(q)$ is the screened dielectric function at momentum q. Here we simply adopt the (two-dimensional) Thomas-Fermi approximation (see the Supplemental Material [40] Sec. III) $\epsilon(q) \approx \epsilon_I(1 + q_{\mathrm{TF}}/q)$, where $\epsilon_I \approx 2 \sim 10$ is the dielectric constant of undoped graphene, and $q_{\mathrm{TF}} \approx 2\pi e^2(\partial n_e/\partial\mu)/\epsilon_I = 2\pi e^2 N_D/\epsilon_I$ is the Thomas-Fermi momentum (n_e and μ are the electron density and chemical potential, respectively). With $N_D \gtrsim 1$ meV^{-1} Ω_s^{-1} around the magic angle, $q_{\mathrm{TF}} \gtrsim 50 k_\theta \gg q$, so the screened Coulomb potential $\mathcal{V}_e(q) \approx 2\pi e^2/\epsilon_I q_{\mathrm{TF}} \sim N_D^{-1}$, yielding a Coulomb coupling strength $\mu_c \approx N_D \mathcal{V}_e(q) \sim 1$. If we adopt the McMillan formula for superconductor T_c [51,52], taking $\lambda = 1.5$ and $\mu_c = 1$, we obtain

$$T_c = \frac{\hbar\omega_D}{1.45 k_B} \exp\left(-\frac{1.04(1+\lambda)}{\lambda - \mu_c^*(1+0.62\lambda)}\right) \approx 0.9 \text{ K} \qquad (10)$$

at the magic angle, where $\mu_c^* = \mu_c/[1 + \mu_c \ln(\omega_{pe}/\omega_D)]$ is the reduced Coulomb coupling strength, and ω_{pe} is the plasma frequency, which is roughly $\hbar\omega_{pe} \sim \sqrt{(4\pi n_e)^{1/2} e^2 \epsilon_F/\epsilon_I} \sim 10\hbar\omega_D$ [53,54]. This agrees well with the experimentally observed T_c. We do emphasize that our T_c estimation is very rough, with inaccuracies from both λ, μ_c^*, and the McMillan formula itself for large λ.

The above electron-phonon coupling calculation can be easily generalized to other twist angles and electron densities. We still keep only the nearest momentum hoppings in the continuum model of TBG, but truncate the Hamiltonian at sufficiently high momentum to obtain more accurate band structures. We then numerically calculate the energy change in each electron band under small deformations of $\mathbf{q}_j$, and verify it is comparable to our *ab initio* results (see the Supplemental Material [40] Sec. V). Subtracting the contribution from moiré BZ deformations (see the Supplemental Material [40] Sec. IV), we can estimate the electron-phonon coupling of each band and the BCS coupling strength $\lambda \approx N_D V_{\mathbf{k}\mathbf{k}}$.

Figures 4(a) and 4(b) show the DOS N_D and BCS coupling strength λ with respect to the number of electrons per superlattice unit cell $n = n_e \Omega_s$ at $\theta = 1.05°$. The DOS is predominantly high for the first conduction and valence bands ($|n| < 4$). However, the BCS coupling λ for $|n| < 4$ and for $|n| > 4$ are of the same order, despite the fact that the DOS is much lower ($N_D \sim 0.05$ meV^{-1} Ω_s^{-1}) at $|n| > 4$. This is because, for higher Moiré bands which have larger band widths, their energy susceptibility to deformations is also larger. For bands with band widths $E_W \gtrsim w$, an order estimation from perturbation theory yields a BCS coupling strength $\lambda \sim [(N_D z^2 w^4)/(M c_T^2 E_W^2)] \sim 0.5$, where $z = 3$ is the number of nearest hopping momenta $\mathbf{q}_j$ (see the Supplemental Material [40] Sec. IV). This agrees with the numerical magnitude in Fig. 4(b), and implies possible BCS superconductivity at higher $|n|$. Figure 4(c) shows T_c from the McMillan formula with respect to angle θ and number of electrons per unit cell n. There is only a narrow superconducting region at $|n| < 4$ near the magic angle, which corresponds to the superconductivity observed in TBG. In contrast, superconductivity of order 1 K may occur in a wide range of $\theta \gtrsim 1°$ for $|n|$ near 8 and higher, which has not been carefully explored yet [55–59], and we expect to be tested in future experiments. There are also parameter spaces for $\theta < 1°$ where T_c is of order of $1K$, e.g., $4 \lesssim |n| \lesssim 8$ near $\theta = 0.8°$, $2 \lesssim |n| \lesssim 12$ near $\theta = 0.6°$, and $8 \lesssim |n| \lesssim 12$ around $\theta = 0.3°$. The vast superconductivity region indicates that the moiré pattern generically enhances the

electron-phonon coupling of all bands, and may explain the possible superconductivity of HOPG. However, we do note that other orders such as charge density wave may compete with superconductivity in these parameter regimes.

Lastly, we comment that the strong phonon-mediated attraction may favor a Bose-Mott insulator [39] for the TBG insulating phase observed at $|n| = 2$ [1,2]. This is because the attraction may pair the electrons into charge $2e$ bosons (Cooper pairs), and for $|n| = 2$, the system has one boson per unit cell and, thus, may form a Bose-Mott insulator [39], with a possible charge density wave order. Such a phase will have a resistivity around $h/(2e)^2 \approx 6k\Omega$ at the superconductor-insulator transition, due to charge $2e$ carriers [60–62]. However, the experimentally observed quantum oscillations [1] indicates these Cooper pairs have to break down for magnetic fields above 1T, if this explanation is correct.

The first-principles calculations performed for this Letter were supported by the Department of Energy Grant No. DE-SC0016239. B. L. is supported by Princeton Center for Theoretical Science at Princeton University. Z. W. acknowledges the support from the CAS Pioneer Hundred Talents Program. B. B. is supported by the Department of Energy Grant No. DE-SC0016239, the National Science Foundation EAGER Grant No. DMR 1643312, Simons Investigator Grants No. 404513, No. ONR N00014-14-1-0330, and No. NSF-MRSEC DMR-142051, the Packard Foundation, and the Schmidt Fund for Innovative Research.

[1] Y. Cao, V. Fatemi, S. Fang, K. Watanabe, T. Taniguchi, E. Kaxiras, and P. Jarillo-Herrero, Unconventional superconductivity in magic-angle graphene superlattices, Nature (London) **556**, 43 (2018).

[2] Y. Cao, V. Fatemi, A. Demir, S. Fang, S. L. Tomarken, J. Y. Luo, J. D. Sanchez-Yamagishi, K. Watanabe, T. Taniguchi, E. Kaxiras, R. C. Ashoori, and P. Jarillo-Herrero, Correlated insulator behaviour at half-filling in magic-angle graphene superlattices, Nature (London) **556**, 80 (2018).

[3] E. Suárez Morell, J. D. Correa, P. Vargas, M. Pacheco, and Z. Barticevic, Flat bands in slightly twisted bilayer graphene: Tight-binding calculations, Phys. Rev. B **82**, 121407(R) (2010).

[4] R. Bistritzer and A. H. MacDonald, Moiré bands in twisted double-layer graphene, Proc. Natl. Acad. Sci. U.S.A. **108**, 12233 (2011).

[5] N. F. Q. Yuan and L. Fu, Model for the metal-insulator transition in graphene superlattices and beyond, Phys. Rev. B **98**, 045103 (2018).

[6] H. Chun Po, L. Zou, A. Vishwanath, and T. Senthil, Origin of Mott Insulating Behavior and Superconductivity in Twisted Bilayer Graphene, Phys. Rev. X **8**, 031089 (2018).

[7] C. Xu and L. Balents, Topological Superconductivity in Twisted Multilayer Graphene, Phys. Rev. Lett. **121**, 087001 (2018).

[8] B. Roy and V. Juričić, Unconventional superconductivity in nearly flat bands in twisted bilayer graphene, Phys. Rev. B **99**, 121407(R) (2019).

[9] G. E. Volovik, Graphite, graphene and the flat band superconductivity, JETP Lett. **107**, 516 (2018).

[10] B. Padhi, C. Setty, and P. W. Phillips, Doped twisted bilayer graphene near magic angles: Proximity to Wigner crystallization, Not Mott insulation, Nano Lett. **18**, 6175 (2018).

[11] J. F. Dodaro, S. A. Kivelson, Y. Schattner, X. Q. Sun, and C. Wang, Phases of a phenomenological model of twisted bilayer graphene, Phys. Rev. B **98**, 075154 (2018).

[12] G. Baskaran, Theory of emergent Josephson lattice in neutral twisted bilayer graphene (Moiŕe is different), arXiv:1804.00627.

[13] F. Wu, A. H. MacDonald, and I. Martin, Theory of Phonon-Mediated Superconductivity in Twisted Bilayer Graphene, Phys. Rev. Lett. **121**, 257001 (2018).

[14] H. Isobe, N. F. Q. Yuan, and L. Fu, Unconventional Superconductivity and Density Waves in Twisted Bilayer Graphene, Phys. Rev. X **8**, 041041 (2018).

[15] T. Huang, L. Zhang, and T. Ma, Antiferromagnetically ordered mott insulator and d + id superconductivity in twisted bilayer graphene: A quantum monte carlo study, Sci. Bull. **64**, 310 (2019).

[16] Y.-Z. You and A. Vishwanath, Superconductivity from valley fluctuations and approximate SO(4) symmetry in a weak coupling theory of twisted bilayer graphene, npj Quantum Mater. **4**, 16 (2019).

[17] X.-C. Wu, K. A. Pawlak, C.-M. Jian, and C. Xu, Emergent superconductivity in the weak Mott insulator phase of bilayer graphene Moiŕe superlattice, arXiv:1805.06906.

[18] Y.-H. Zhang, D. Mao, Y. Cao, P. Jarillo-Herrero, and T. Senthil, Nearly flat chern bands in moiré superlattices, Phys. Rev. B **99**, 075127 (2019).

[19] J. Kang and O. Vafek, Symmetry, Maximally Localized Wannier States, and a Low-Energy Model for Twisted Bilayer Graphene Narrow Bands, Phys. Rev. X **8**, 031088 (2018).

[20] M. Koshino, N. F. Q. Yuan, T. Koretsune, M. Ochi, K. Kuroki, and L. Fu, Maximally Localized Wannier Orbitals and the Extended Hubbard Model for Twisted Bilayer Graphene, Phys. Rev. X **8**, 031087 (2018).

[21] D. M. Kennes, J. Lischner, and C. Karrasch, Strong correlations and $d + id$ superconductivity in twisted bilayer graphene, Phys. Rev. B **98**, 241407(R) (2018).

[22] L. Zhang, Lowest-energy moire band formed by dirac zero modes in twisted bilayer graphene, Sci. Bull. **64**, 495 (2019).

[23] J. M. Pizarro, M. J. Calderón, and E. Bascones, The nature of correlations in the insulating states of twisted bilayer graphene, J. Phys. Commun. **3**, 035024 (2019).

[24] F. Guinea and N. R. Walet, Electrostatic effects, band distortions, and superconductivity in twisted graphene bilayers, Proc. Natl. Acad. Sci. U.S.A. **115**, 13174 (2018).

[25] A. Thomson, S. Chatterjee, S. Sachdev, and M. S. Scheurer, Triangular antiferromagnetism on the honeycomb lattice of twisted bilayer graphene, Phys. Rev. B **98**, 075109 (2018).

[26] M. Ochi, M. Koshino, and K. Kuroki, Possible correlated insulating states in magic-angle twisted bilayer graphene under strongly competing interactions, Phys. Rev. B **98**, 081102(R) (2018).

[27] X. Yan Xu, K. T. Law, and P. A. Lee, Kekulé valence bond order in an extended hubbard model on the honeycomb lattice with possible applications to twisted bilayer graphene, Phys. Rev. B **98**, 121406(R) (2018).

[28] T. J. Peltonen, R. Ojajärvi, and T. T. Heikkilä, Mean-field theory for superconductivity in twisted bilayer graphene, Phys. Rev. B **98**, 220504(R) (2018).
[29] M. Fidrysiak, M. Zegrodnik, and J. Spałek, Unconventional topological superconductivity and phase diagram for an effective two-orbital model as applied to twisted bilayer graphene, Phys. Rev. B **98**, 085436 (2018).
[30] L. Zou, H. Chun Po, A. Vishwanath, and T. Senthil, Band structure of twisted bilayer graphene: Emergent symmetries, commensurate approximants, and wannier obstructions, Phys. Rev. B **98**, 085435 (2018).
[31] J. González and T. Stauber, Kohn-Luttinger Superconductivity in Twisted Bilayer Graphene, Phys. Rev. Lett. **122**, 026801 (2019).
[32] Y. Su and S.-Z. Lin, Pairing symmetry and spontaneous vortex-antivortex lattice in superconducting twisted-bilayer graphene: Bogoliubov-de gennes approach, Phys. Rev. B **98**, 195101 (2018).
[33] H. Guo, X. Zhu, S. Feng, and R. T. Scalettar, Pairing symmetry of interacting fermions on a twisted bilayer graphene superlattice, Phys. Rev. B **97**, 235453 (2018).
[34] Z. Song, Z. Wang, W. Shi, G. Li, C. Fang, and B. A. Bernevig, All "Magic Angles" Are "Stable" Topological, arXiv:1807.10676.
[35] P. Esquinazi, Invited review: Graphite and its hidden superconductivity, Pap. Phys. **5**, 050007 (2013).
[36] A. Ballestar, J. Barzola-Quiquia, T. Scheike, and P. Esquinazi, Josephson-coupled superconducting regions embedded at the interfaces of highly oriented pyrolytic graphite, New J. Phys. **15**, 023024 (2013).
[37] A. Ballestar, T. T. Heikkilä, and P. Esquinazi, Size dependence of the josephson critical behavior in pyrolytic graphite tem lamellae, Supercond. Sci. Technol. **27**, 115014 (2014).
[38] P. Esquinazi, T. T. Heikkilä, Y. V. Lysogorskiy, D. A. Tayurskii, and G. E. Volovik, On the superconductivity of graphite interfaces, JETP Lett. **100**, 336 (2014).
[39] M. P. A. Fisher, P. B. Weichman, G. Grinstein, and D. S. Fisher, Boson localization and the superfluid-insulator transition, Phys. Rev. B **40**, 546 (1989).
[40] See Supplemental Material at http://link.aps.org/supplemental/10.1103/PhysRevLett.122.257002, including a Supplemental Video, for detailed derivation of the electron phonon coupling, numerical calculation of phonon interaction in higher bands and *ab initio* calculations under deformations, which includes Refs. [41–47].
[41] L. D. Landau, L. P. Pitaevskii, A. M. Kosevich, and E. M. Lifshitz, *Theory of Elasticity* (Butterworth-Heinemann, London, 2012).
[42] P. E. Blöchl, Projector augmented-wave method, Phys. Rev. B **50**, 17953 (1994).
[43] G. Kresse and D. Joubert, From ultrasoft pseudopotentials to the projector augmented-wave method, Phys. Rev. B **59**, 1758 (1999).
[44] G. Kresse and J. Hafner, Ab initio molecular dynamics for liquid metals, Phys. Rev. B **47**, 558 (1993).
[45] G. Kresse and J. Furthmller, Efficiency of ab-initio total energy calculations for metals and semiconductors using a plane-wave basis set, Comput. Mater. Sci. **6**, 15 (1996).
[46] P. Hohenberg and W. Kohn, Inhomogeneous electron gas, Phys. Rev. **136**, B864 (1964).
[47] J. M. B. Lopes dos Santos, N. M. R. Peres, and A. H. Castro Neto, Graphene Bilayer with a Twist: Electronic Structure, Phys. Rev. Lett. **99**, 256802 (2007).
[48] A. I. Cocemasov, D. L. Nika, and A. A. Balandin, Phonons in twisted bilayer graphene, Phys. Rev. B **88**, 035428 (2013).
[49] P. W. Anderson, Theory of dirty superconductors, J. Phys. Chem. Solids **11**, 26 (1959).
[50] Y. Woo Choi and H. Joon Choi, Strong electron-phonon coupling, electron-hole asymmetry, and nonadiabaticity in magic-angle twisted bilayer graphene, Phys. Rev. B **98**, 241412(R) (2018).
[51] W. L. McMillan, Transition temperature of strong-coupled superconductors, Phys. Rev. **167**, 331 (1968).
[52] P. B. Allen and R. C. Dynes, Transition temperature of strong-coupled superconductors reanalyzed, Phys. Rev. B **12**, 905 (1975).
[53] E. H. Hwang and S. Das Sarma, Dielectric function, screening, and plasmons in two-dimensional graphene, Phys. Rev. B **75**, 205418 (2007).
[54] S. Das Sarma and E. H. Hwang, Collective Modes of the Massless Dirac Plasma, Phys. Rev. Lett. **102**, 206412 (2009).
[55] K. Kim, A. DaSilva, S. Huang, B. Fallahazad, S. Larentis, T. Taniguchi, K. Watanabe, B. J. LeRoy, A. H. MacDonald, and E. Tutuc, Tunable moiré bands and strong correlations in small-twist-angle bilayer graphene, Proc. Natl. Acad. Sci. U.S.A. **114**, 3364 (2017).
[56] D. Wong, Y. Wang, J. Jung, S. Pezzini, A. M. DaSilva, H.-Z. Tsai, H. Sae Jung, R. Khajeh, Y. Kim, J. Lee, S. Kahn, S. Tollabimazraehno, H. Rasool, K. Watanabe, T. Taniguchi, A. Zettl, S. Adam, A. H. MacDonald, and M. F. Crommie, Local spectroscopy of moiré-induced electronic structure in gate-tunable twisted bilayer graphene, Phys. Rev. B **92**, 155409 (2015).
[57] M. Yankowitz, S. Chen, H. Polshyn, Y. Zhang, K. Watanabe, T. Taniguchi, David Graf, A. F. Young, and C. R. Dean, Tuning superconductivity in twisted bilayer graphene, Science **363**, 1059 (2019).
[58] A. Kerelsky, L. McGilly, D. M. Kennes, L. Xian, M. Yankowitz, S. Chen, K. Watanabe, T. Taniguchi, J. Hone, C. Dean, A. Rubio, and A. N. Pasupathy, Magic Angle Spectroscopy, arXiv:1812.08776.
[59] Y. Choi, J. Kemmer, Y. Peng, A. Thomson, H. Arora, R. Polski, Y. Zhang, H. Ren, J. Alicea, G. Refael, F. von Oppen, K. Watanabe, T. Taniguchi, and S. Nadj-Perge, Imaging electronic correlations in twisted bilayer graphene near the magic angle, arXiv:1901.02997.
[60] M. P. A. Fisher, G. Grinstein, and S. M. Girvin, Presence of Quantum Diffusion in Two Dimensions: Universal Resistance at the Superconductor-Insulator Transition, Phys. Rev. Lett. **64**, 587 (1990).
[61] A. Yazdani and A. Kapitulnik, Superconducting-Insulating Transition in Two-Dimensional a-Moge Thin Films, Phys. Rev. Lett. **74**, 3037 (1995).
[62] M. A. Steiner, N. P. Breznay, and A. Kapitulnik, Approach to a superconductor-to-bose-insulator transition in disordered films, Phys. Rev. B **77**, 212501 (2008).

Correction: The omission of a support statement in the Acknowledgments section has been fixed.